Ab initio study of the stabilities of and mechanism of superionic transport in lithium-rich antiperovskites

Yi Zhang, Yusheng Zhao, and Changfeng Chen

Phys. Rev. B **87**, 134303 — Published 29 April 2013

DOI: 10.1103/PhysRevB.87.134303

Stability and mechanism of superionic transport of lithium-rich anti-perovskites

Yi Zhang, Yusheng Zhao, and Changfeng Chen
Department of Physics and High Pressure Science and Engineering Center, University of Nevada, Las Vegas, Nevada 89154, USA
(Dated: March 11, 2013)

Recently, a family of halogen-based Li-rich anti-perovskites was synthesized [J. Am. Chem. Soc. **134**, 15042 (2012)], and the measured superionic conductivity makes these materials promising candidates as solid electrolytes for applications in Li-ion and Li-air batteries. This discovery raises several pressing issues on the fundamental physics concerning the thermodynamic and electrochemical stability of the synthesized materials and the mechanism of the observed superionic Li^+ transport. Here we study the reported anti-perovskites Li_3OCl, Li_3OBr and their mixed compounds using first-principles density functional theory and molecular dynamics simulations. Our calculations show that these materials are thermodynamically metastable. Their large electronic band gaps and chemical stability against electrodes suggest the excellent electrochemical performance, which bodes well for the use in potentially harsh working conditions in practical battery applications. The calculated low activation enthalpy for Li ion migration well below the crystal melting temperature and superionic transport near the Li sub-lattice melting state explain the experimentally observed phenomena. Our study identifies mobile Li vacancies and anion disorder as the primary driving mechanisms for superionic Li^+ conductivity in the anti-perovskites. The present work unveils essential working principles of the Li-rich anti-perovskites, which are crucial to further exploration, development, and application of these and other charge-inverted materials with tailored properties.

PACS numbers: 66.30.H-, 82.47.Aa, 82.60.-s

I. INTRODUCTION

Solids with superionic conductance are promising replacements for current organic liquid electrolytes in battery applications[1]. Li-rich solid electrolytes have received special interest because of their good safety features and high energy density and power capacity. There have been concerted efforts in search of solid Li electrolytes of diverse structural forms, including crystalline, glassy, polymer, and composite[2–6] Most solid Li-electrolyte materials, however, suffer from low Li^+ ion conductivity, or small operating voltage windows, or both which prevent them from being used in large scale applications. Recently, inspired by high-temperature superionic conductivity in fluorine-rich perovskite $NaMgF_3$[7], $CsPbF_3$[8], and $KMnF_3$[9], a family of anti-perovskites, e.g., Li_3OCl, Li_3OBr, and their mixed compound $Li_3OCl_{0.5}Br_{0.5}$, has been designed and synthesized[10]. As the charge-inverted isostructural forms of fluorine-rich perovskites, these anti-perovskites exhibit superionic Li^+ conductivity and low electrical conductivity. Moreover, their complex crystal structures allow a considerable degree of structural manipulation to tailor the electronic and transport properties. This line of research may open a productive avenue for exploring efficient solid electrolytes for battery applications.

The interesting physical phenomenon of superionic transport can be understood as fast ion hopping through favorable pathways in a structural framework. The available ion transport pathways are critical to superionic conductivity, and they are very sensitive to the details of the crystal structure of different materials. Superionic conduction usually occurs at high temperatures accompanied by an order-disorder transition of the ion sub-lattice. Such a phase transition, known as partial melting, can be driven by soft phonon modes, lattice strain, or structural disorder. Previous studies[11–13] showed that ionic conductivity could be improved significantly by tuning these driving forces. For practical applications, it is crucial that the recently synthesized anti-perovskites exhibit good thermodynamic and electrochemical stability. Another critical issue concerns the primary mechanisms for the observed fast Li^+ transport that holds the key to improving the performance of current materials and design of new ones. In-depth understanding of these important issues, however, has been impeded by the complicated synthesis and measurement conditions employed in the experimental procedures[10]. It is therefore critical that we explore these materials and physical phenomena by reliable theoretical approaches to shed light on the main physics and answer the fundamental questions concerning stability and mechanism of superionic conductivity in this family of promising materials.

In this work, we employ first-principles density functional theory (DFT) calculations to investigate the crystal structure and stability of Li_3OCl, Li_3OBr, and their mixed compound $Li_3OCl_{0.5}Br_{0.5}$ composite. Our results indicate that these materials are metastable thermodynamically but electrochemically very stable. We also use *ab initio* molecular dynamics (AIMD) simulations to explore possible mechanism of superionic Li^+ conduction in these materials. We observe in our AIMD simulations Li sub-lattice melting associated with the fast Li^+ ion transport, which reveals the underlying mechanism for the observed superionic conductivity. This partial sub-lattice melting occurs well below the melting temperature of the anti-perovskites, which agrees with experimental observation. A close analysis identifies mo-

bile Li vacancy and anion disorder as the main driving forces for the superioninc conductivity in these materials. Our results establish the fundamental physics and basic working principles of the recently discovered anti-perovskites, which should help further explore more complicated structural and transport properties of these materials and provide useful insights for synthesis and study of additional charge-inverted materials as potential superionic conductors.

II. COMPUTATIONAL METHOD

We carried out first-principles DFT calculations adopting the Perdew-Burke-Ernzerhof generalized gradient approximation (GGA)[14] as implemented in the Vienna *ab initio* simulation package (VASP)[15]. We used the projector augmented wave (PAW)[16] pseudopotential method with a plane wave basis set and a cutoff energy of 400 eV, and employed a 16×16×16 Monkhorst-Pack[17] k-point grid in total energy and electronic density of states calculations. For supercell calculations, we used a 2×2×2 k-grid, and achieved a total energy convergence within 0.2 meV per atom when comparing the results with those using denser grids. The electronic steps are carried out with the energy convergence on the order of 10^{-6} eV, and the force convergence of ionic steps is set to 10^{-2} eV/Å. The Li^+ ion hopping barriers are obtained using the climbing image nudged elastic band (CINEB) method[18], which can efficiently determine the pathway for structural changes[19–21]. To study Li-ion transport, we performed AIMD simulations using a 2×2×2 (40 atoms) supercell and a 2 fs time step. Each AIMD simulation lasts for 80 ps after a 10-ps pre-equilibrium run. Elevated temperatures up to 2,000 K were applied to speed up the ion-hopping process in a fixed unit-cell volume, thus shortening the simulation time. While this approach is suitable for evaluating ion activation enthalpy and identifying ion transport mechanism[22,23], such canonical ensemble (NVT) AIMD simulations overestimate the melting temperature (T_m) significantly since the effect of thermal expansion is not included. To simulate actual thermal expansion and crystal melting, we ran additional AIMD simulations where the structure is allowed to fully relax at each temperature point such that all the MD average residual components of the Hellmann-Feymann stress tensor and the average force on each atom are less than 0.5 GPa and 0.01 eV/Å, respectively. The shape of the supercell and the average atomic positions are determined by atomic relaxation.

To study superionic transport in the anti-perovskites, we have calculated the diffusion coefficient for Li^+ transport and the mean square displacement (MSD) of the ionic positions. The diffusion coefficient is defined as

$$D = \lim_{t\to\infty}[\frac{1}{2dt}\langle[\vec{r}(t)]^2\rangle], \tag{1}$$

where d is the dimension of the lattice on which ion hopping takes place. The MSD

$$\langle[\vec{r}(t)]^2\rangle = \frac{1}{N}\sum_{i=1}^{N}\langle[\vec{r_i}(t+t_0) - \vec{r_i}(t_0)]^2\rangle \tag{2}$$

is averaged over all Li^+ ions, and $\vec{r_i}(t)$ is the displacement of the i-th Li^+ ion at time t, and N is the total number of Li^+ ions in the system. In practice, D is obtained by a linear fit to the time dependence of average MSD. Convergence of D can be achieved within 80 ps due to the fast ionic processes in the simulated materials.

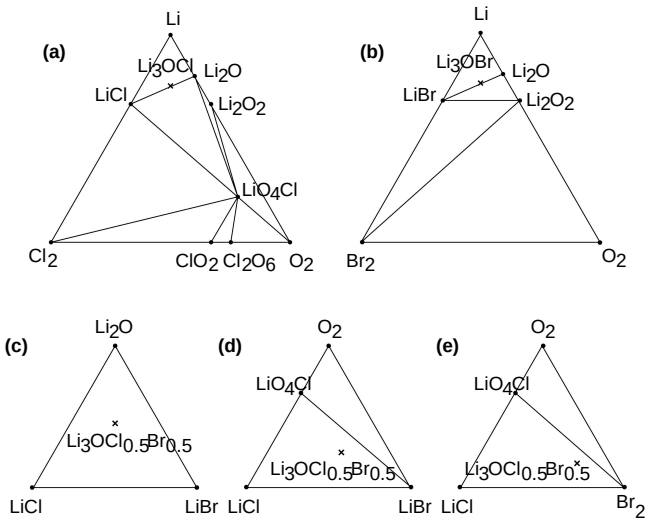

FIG. 1: Calculated ternary phase diagram of (a) Li-O-Cl and (b) Li-O-Br systems and phase evolution of the Li-O-Cl-Br system at (c) μ_{Li} = 0 eV, (d) μ_{Li} = -2.9 eV, and (e) μ_{Li} = -3.2 eV. The stability of the compound (marked with a black cross) is determined by the stable phases at the vertices of triangle surrounding the compound.

III. RESULTS AND DISCUSSION

A. Crystal Structure and Stability

The Li-rich anti-perovskites are designed as a charge-inverted counterpart of superionic F^- conductor $NaMgF_3$ that has the typical $A^+B^{2+}X_3{}^-$ perovskite structure. To construct the isostructural Li-rich anti-perovskites, one starts by replacing the monovalent octahedral vertex F^- sites by electropositive Li^+ ions, and continuing the charge inversion on the other sites makes the new $X_3{}^+B^{2-}A^-$ anti-perovskites[10]. The divalent element at the octahedral center B site is chosen to be oxygen and the monovalent element at the dodecahedral A site can be any halogen. In the present work, following the recently reported synthesis[10], we construct the crystal structures of Li_3OCl, Li_3OBr, and $Li_3OCl_{0.5}Br_{0.5}$, denoted as LOC, LOB, and LOCB, respectively, in analogy to $NaMgF_3$ and (K, Na)MgF_3. We consider two independent atomic arrangements in a 40-atom LOCB supercell:

TABLE I: Calculated lattice parameters of $NaMgF_3$, Li_3OCl (LOC), Li_3OBr (LOB), and $Li_3OCl_{0.5}Br_{0.5}$ (LOCB) compared with available experimental data.

		Symmetry	a (Å)	b (Å)	c (Å)
$NaMgF_3$	Calc.	Pnma	5.3336	5.5074	7.6510
	Expt.[a]	Pnma	5.3650	5.4920	7.6740
Li_3OCl	Calc.	$Pm\bar{3}m$	3.8496	3.8496	3.8496
	Expt.[b]	$Pm\bar{3}m$	3.91	3.91	3.91
Li_3OBr	Calc.	$Pm\bar{3}m$	3.9806	3.9806	3.9806
	Expt.[b]	$Pm\bar{3}m$	4.02	4.02	4.02
LOCB1	Calc.	$Fm\bar{3}m$	7.8129	7.8129	7.8129
LOCB2	Calc.	P4/mmm	3.9351	3.9351	7.8699

[a][24]
[b][10]

(i) LOCB1 that has $Fm\bar{3}m$ cubic symmetry with the Cl and Br anions occupy 4a(0, 0, 0) and 4b(0.5, 0, 0) sites, respectively; (ii) LOCB2 in P4/mmm tetragonal symmetry where the Cl-Li and Br-Li layers are separated by the O-Li layers along the [001] direction. Many perovskites undergo a distortion away from the high symmetry cubic structure. To include this possibility, we set the initial unit cells of all four structures to orthorhombic with the atomic positions deviated slightly from the ideal lattice positions. These structures become pseudo-cubic after a full relaxation. Unlike $NaMgF_3$ that contains tilting MgF_6 octahedra, no tilting of the Li_6O octahedra is seen in the relaxed structures. The calculated lattice parameters for $NaMgF_3$, LOC, LOB, LOCB1, and LOCB2 are summarized in Table I. The excellent agreement with experimental data[10,24] lends confidence to our structural modeling and computational approach.

We constructed the ternary Li-O-Cl and Li-O-Br phase diagrams using all known Li-O-Cl and Li-O-Br compounds in the Landolt-Börnstein database[25]. Only the thermodynamically stable phases and the calculated ground states of LOC and LOB are considered. In Fig. 1, filled circles represent stable compounds with lower energy than a linear combination of other structures with the same chemical composition. Our phase diagram calculations (at 0K) predict that LOC and LOB are energetically unstable with respect to the following reactions:

$$Li_3OCl \rightarrow Li_2O + LiCl, \quad (3)$$

$$Li_3OBr \rightarrow Li_2O + LiBr. \quad (4)$$

Nevertheless, these materials could be metastable or stabilized by pressure[26] or entropy at room temperature since the formation energy for reactions described in Eqs.(1) and (2) are only -13.9 and -25.8 meV/atom. No preference of Br/Cl ordering is seen in the LOCB compound, and the energy difference between LOCB1 and LOCB2 is only 1.6 meV/atom. Since the mixing of Br and Cl occupations increases the energy by only a few meV/atom, the decomposition tendency of LOCB towards LOC and LOB is expected to be weak.

Good solid Li-electrolytes must remain stable and electrically conductive in contact with the electrode materials. To investigate the chemical stability of anti-perovskites under extreme Li insertion and extraction conditions, we constructed the lithium grand potential phase diagram of Li-O-Cl, Li-O-Br, and Li-O-Cl-Br using the method outlined by Ong *et al.*[27]. By studying the phase evolution of the LOC, LOB, and LOCB compounds with the changing chemical potential (μ_{Li}), we determine the equilibrium phases at bulk metallic lithium anode and charged cathode. The chemical potential of bulk lithium metal is set to zero and the voltage is the negative of μ_{Li}. On the anode side ($\mu_{Li} = 0$ eV), the LOC and LOB follow the reactions in Eq. 3 and 4. Li_2O was reported to be a fast ionic conductor[28]. Therefore, we expect the Li_2O and LiX (X= Cl, Br) mixture may form a conductive layer between anode and electrolyte even if the anti-perovskites are unstable against lithium metal at ambient or higher temperature. On the cathode side, phase equilibria of LOC at -3.6 eV$< \mu_{Li} <$ -2.9 eV and LOB at -3.2 eV $< \mu_{Li} <$ -2.7 eV comprise LiCl and LiO_4Cl, and LiBr and Li_2O_2, respectively. However, higher voltage decompositions of LOC and LOB at $\mu_{Li} <$ -4.0 eV lead to undesired Cl_2, ClO_2, and Br_2, which could cause problems in battery application. In Fig.1 (c-e), the phase diagrams of Li-O-Cl-Br system are plotted at three representative lithium chemical potential to show the changes of phase equilibria. With the decreasing μ_{Li}, the LOCB compound evolves as if the mixture of LOC and LOB. At $\mu_{Li} = 0$ eV, the LOCB decomposes to LiCl, LiBr, and Li_2O. When μ_{Li} is lower than -2.9 eV, LiO_4Cl begins to appear as the oxygen-containing phase. At even lower μ_{Li} = -3.2 eV, the LOCB decomposes to LiCl, LiO_4Cl, and Br_2.

We next examine the electrochemical windows of LOC, LOB, and LOCB adopting the approach by Ong *et al.*[29], which calculates the density of states (DOS) of the material to determine the energies of the lowest unoccupied molecular orbital (LUMO) and the highest occupied molecular orbital (HOMO). The band gap assessment provides the upper limit of electrochemical stability on inert electrodes. Due to the well-known underestimation of the GGA method in band gap calculations, we calculated the DOS using the Heyd-Scuseria-Erznerhof (HSE06) functional[30]. The calculated results plotted in Fig. 2 show that the band gaps of all the compounds studied here are around 5 eV. This is in stark contrast to many known crystalline materials with small band gaps and high ionic conductivity that suffer from poor electrochemical stabilities[31,32]. The calculated large band gaps may suggest the excellent electrochemical stability of the Li-rich anti-perovskites, which is ideal for their practical applications.

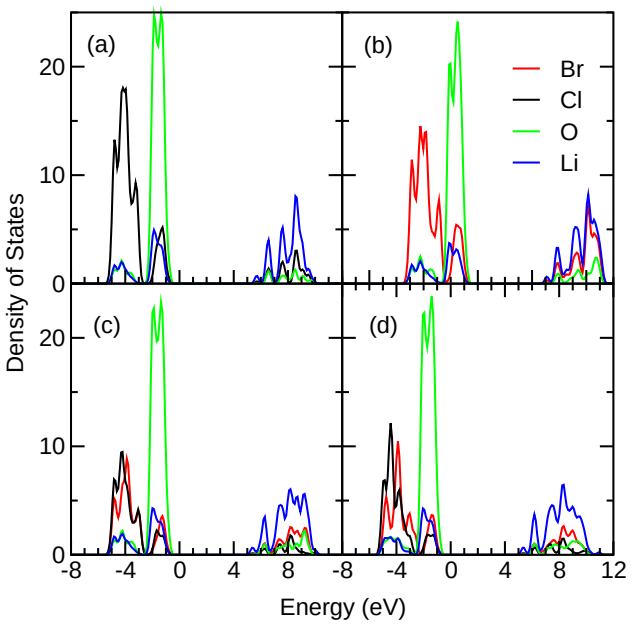

FIG. 2: (Color online) Local-projected DOS of (a) LOC, (b) LOB, (c) LOCB1, and (d) LOCB2 calculated using the HSE06 functional.

B. Lithium ion transport

The mechanism of superionic conductivity in fluoride perovskites have long been debated and remained unresolved with conflicting evidence regarding the behavior of fast F^- ion transport in compounds like $KMgF_3$ and $KCaF_3$[33]. Previous studies[8,34] suggested that the superionic conductivity could be caused by various structural defects since the ideal perovskite structure does not contain unoccupied cation or anion sites. To address this issue for the Li-rich anti-perovskites, we have performed AIMD simulations for both perfect and defective crystals to study the cases of possible Li^+ migration between interstitial sites in perfect crystals and the vacancy-mediated Li^+ transport in defective crystals. For the vacancy-containing case, one Li^+ ion is removed to create a vacancy in the supercell [see Fig. 3(a)] while a uniform charge neutralizing background is imposed automatically by VASP. We also examined the ion-ion interchange mechanism suggested by Cheeseman[34] for $NaMgF_3$ by swapping the positions of a pair of Cl^- and O^{2-} anion in the 40-atom LOC supercell [see Fig. 3(b)]. Cation-anion interchanges are not considered here since they violate the charge balance requirement for structural stability.

Due to the high crystal symmetry of the anti-perovskites, there are only two independent paths for direct Li hopping. One is along the edge of the Li_6O octahedra and the other is between the vertices of two neighboring octahedra. They correspond to path Li_2-Li_1 and Li_3-Li_1 in the enlarged $\sqrt{2}\times\sqrt{2}\times 1$ supercell shown in Fig. 4. The halogen vacancies balance the negative charge of Li vacancies. They do not accept direct incoming Li^+ ion due to the incompatible valence charge. But the resulted residual charge and local lattice distortion may affect the hopping energy of the nearby Li^+ ions. We calculate the energy barriers by moving a Li^+ ion from a nearby site into the vacancy along paths Li_2-V_{Li1} and Li_3-V_{Li1} with and without the presence of the halogen vacancy. The results for LOC and LOB are listed in Table II. Path Li_2-V_{Li1} has lower energy barriers of 0.367 and 0.405 eV for LOC and LOB, respectively. As a comparison, the calculated barrier of path Li_3-V_{Li1} for LOC is 0.834 eV higher, and a 50% increase in barrier height is obtained when the Cl sites are replaced by Br. The effect of Cl and Br vacancies on Li hopping barrier is complicated. For path Li_3-V_{Li1}, the energy barrier is reduced due to the increased free space between the Li sites. For Li_2-V_{Li1}, however, the Cl and Br vacancies lead to an increase of the barrier by ∼0.15 eV. This unexpected result could come from the strong repulsion between the positive residual charge surrounding the halogen vacancy and the nearby mobile Li^+ ions. The ion transport efficiency is dominated by paths with the lowest hopping energy barrier. Therefore, the presence of halogen vacancies does not benefit the fast Li transport in anti-perovskites. At low concentrations, the halogen vacancies should not increase the energy cost of Li migration in the long range as they remain non-diffusive at high temperature.

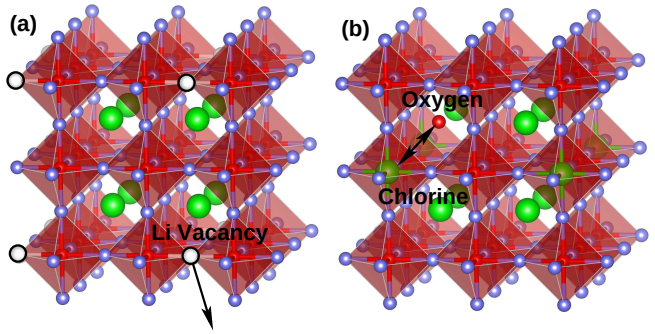

FIG. 3: (Color online) Two structural models for defective anti-perovskites: (a) a Li^+ ion (blue) is removed from the supercell to create a vacancy (white) and (b) a pair (1/8) of chlorine (green) and oxygen (red) anion is exchanged to induce structural disorder.

TABLE II: Calculated Li migration barriers (in eV) for L_3OCl and L_3OBr along selected paths. V_{Li}, V_{Cl}, and V_{Br} represent the Li, Cl, and Br vacancies in the supercell. The ion positions are indicated in Fig. 4.

Vacancy	Path	Li_3OCl	Li_3OBr
V_{Li_1}	$Li_2 \rightarrow V_{Li_1}$	0.367	0.405
V_{Li_1}	$Li_3 \rightarrow V_{Li_1}$	1.201	1.778
$V_{Li_1} - V_{Cl_1}(V_{Br_1})$	$Li_2 \rightarrow V_{Li_1}$	0.513	0.574
$V_{Li_1} - V_{Cl_1}(V_{Br_1})$	$Li_3 \rightarrow V_{Li_1}$	1.005	1.558

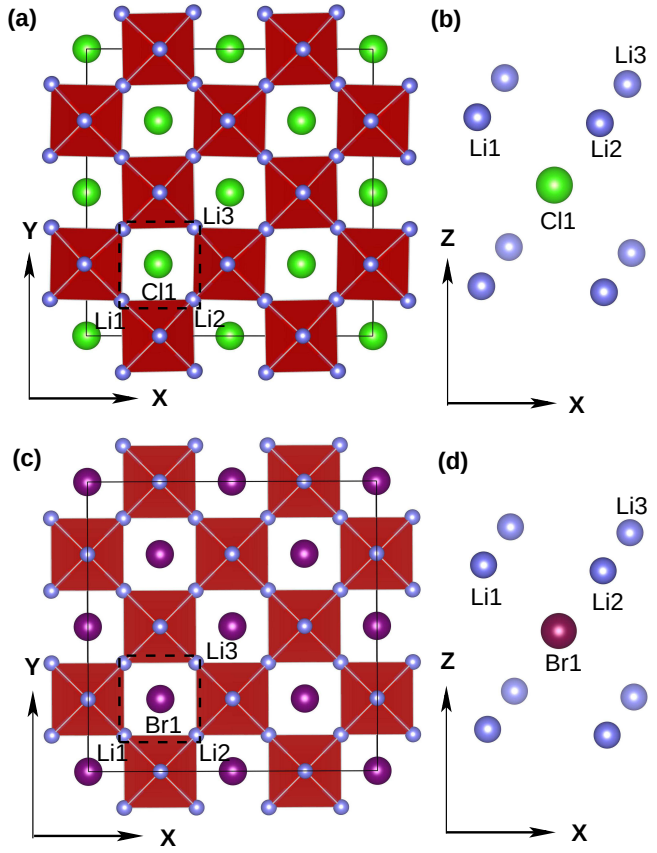

FIG. 4: (Color online) The crystal lattice for (a) LOC and (c) LOB; the local three-dimensional atomic arrangements in the regions outlined by the dashed-line boxes are shown in (b) and (d). The filled spheres in blue, green, and purple represent Li, Cl, and Br atom, respectively. The O atoms stay at the center of the red Li_6O octahedra.

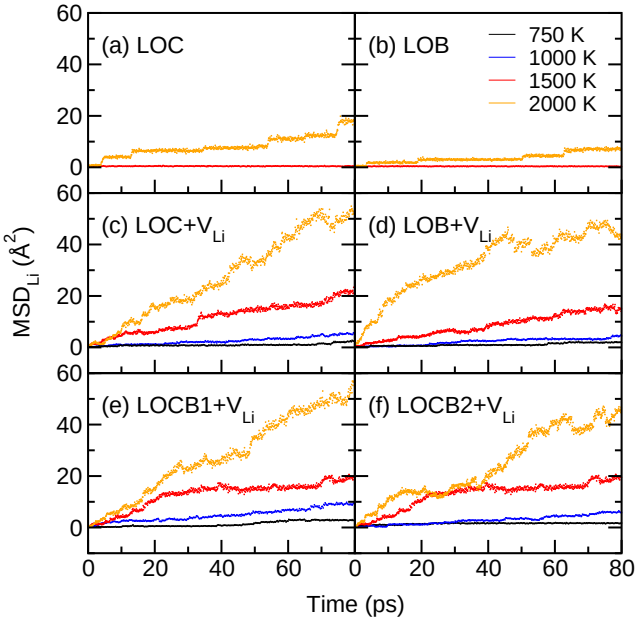

FIG. 5: (Color online) The MSD of Li (MSD_{Li}) as a function of time at different temperatures for (a) LOC, (b) LOB, (c) LOC+V_{Li}, (d) LOB+V_{Li}, (e) LOCB1+V_{Li}, and (f) LOCB2+V_{Li}.

We study the ion mobility by calculating the MSD as a function of time in AIMD simulations. Plotted in Fig. 5 are the calculated MSD for LOC, LOB, and LOCB adopting the elevated temperature (and fixed volume) scheme to speed up the process[22,23]. In the absence of any vacancies [Fig. 5(a) and (b)], no measurable net MSD for Li is seen up to 1,500 K. At 2,000 K, the MSD of Li^+ ions starts to increase drastically. This increase of MSD, however, does not correspond to superionic conductance since the MSD of O and Cl ions also increase with time, which signals the melting of the entire crystal. This result suggests that ideal anti-perovskites are not superionic conductors since their dense crystal structures do not provide pathways for ion transport as commonly seen in superionic conductors[35]. The experimentally synthesized crystal of LOC is distorted and a phase transition was observed in LOCB[10]; these structural imperfections are the likely driving forces for the observed superionic conductivity. To assess these possibilities, we have simulated [see results in Fig. 5(c) and (d)] crystal structures with a Li vacancy in the LOC (LOC+V_{Li}) and LOB (LOB+V_{Li}) supercell, which amounts to a density loss of 1.19% and 0.74%, respectively. It should be noted that although the creation of Li vacancies in the perfect crystals of anti-perovskites is energetically costly, stable Li vacancies can be easily introduced during synthesis through bivalent cation doping or anion removal. In these structurally defective crystals, Li^+ ion transport is observed at a much lower 750 K (compared to those of perfect crystals, but still in the elevated temperature scheme) while the anion sites remain non-diffusive (i.e., no crystal melting). The presence of Li vacancies also accelerates the Li^+ ion migration significantly. At 2,000 K, Li^+ ions diffuse 2.5 times faster in the defective crystals than they do in the perfect crystals. Again, no MSD increase was observed for the anions during the simulation, indicating that the structural integrity of the crystal is maintained. We also examined the mixed LOCB1 and LOCB2 composites with the Li vacancy and obtained results [Fig. 5(e) and (f)] similar to those for LOC and LOB with the Li vacancy.

Fig. 6 shows the trajectories of Li^+ ion in LOC+V_{Li} and LOB+V_{Li} crystals during the MD simulation. At 1,000 K, the Li^+ ions are confined to local vibrations around their lattice positions. There are signs of phonon softening in regions with large vibration magnitude. As temperature increases to 2,000 K, the Li vibration expands in magnitude and the trajectories of neighboring atoms start to overlap, which significantly increases the probability of Li^+ ion hopping toward unoccupied neighboring sites, resulting in the formation of superionic transport channels. An analysis of our simulation results indicates that the nearest-neighbor Li^+ ion hop-

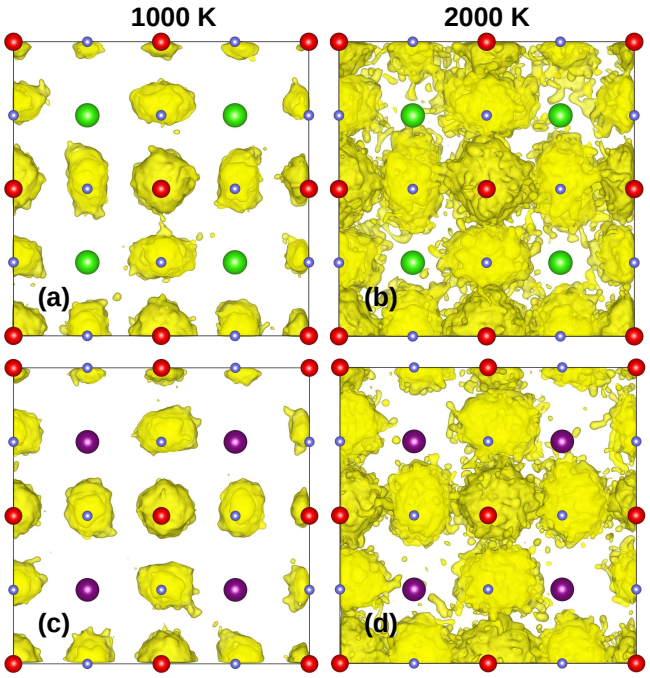

FIG. 6: (Color online) The XY projection (yellow) of Li trajectories in the fixed-volume supercell at 1,000 and 2,000 K for (a-b) LOC+V_{Li} and (c-d) LOB+V_{Li}. The blue, red, green, and purple spheres are initial positions of Li, O, Cl, and Br, respectively.

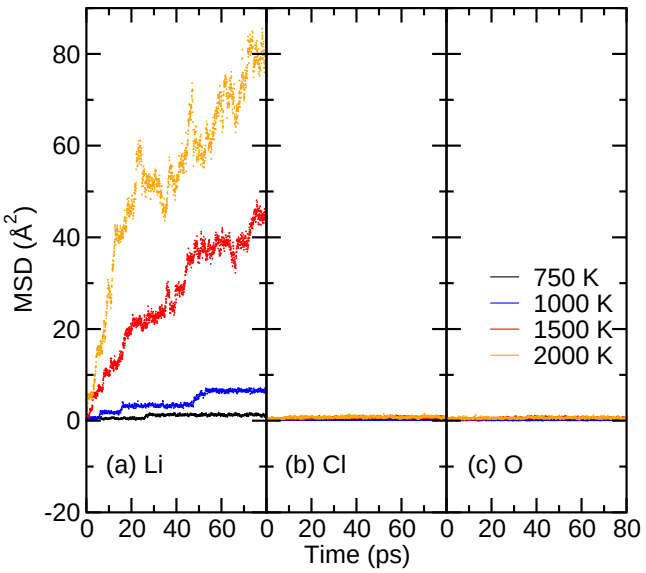

FIG. 7: (Color online) Calculated MSDs of (a) Li, (b) Cl, and (c) O as function of time at different temperatures for the disordered 40-atom LOC supercell with one pair of Cl-O interchanged.

ping occurs along the edge of the Li_6O octahedra and the migration paths are three dimensional. These results are consistent with the energy barrier calculations. The movements of halogen and oxygen anions are quite localized prior to crystal melting, which is because the nearest-neighbor anion sites are well separated by the Li^+ ion, making the anion diffusion rather difficult.

As discussed above, ideal anti-perovskites with perfect crystal structures do not show superionic conductivity. Introducing structural disorder may provide interstitial states for Li migration in vacancy-free crystals at high temperatures. Here we examine the effect of structural disorder by considering a simple model situation with a pair of Cl and O exchanged in the LOC supercell. A similar cation-exchange case has been studied by Cheeseman in $NaMgF_3$[34]. Structural optimization yields a slightly distorted cubic unit cell 3.16% larger than the ideal unit cell. The Li sub-lattice positions are distorted strongly near the exchanged anion center. Results in Fig. 7 show a measurable MSD of Li^+ in the disordered LCO above 750 K. Interestingly, the disordered LOC exhibits even larger MSD_{Li} and therefore Li mobility than the LOC+V_{Li} above 1,000 K. This enhancement can be ascribed to the increased disorder of the Li sub-lattice. Fig. 8 shows the distribution of the trajectory of the Li ions for the ideal and disordered LOC at 1,500 K. Significant Li disorder is seen near the exchanged oxygen anion [Fig. 8(b)], which is similar to the incompletely melted state of the Li sub-lattice. This result contrasts sharply with the case of the ideal crystal [Fig. 8(a)] in which all the Li^+ ions display localized vibration. The average enthalpy gain associated with one Cl-O pair exchange is 74.8 meV/atom, which is too high to realize thermodynamically. Nevertheless, the disordered structure is quite stable under large thermal perturbations. No Cl or O diffusion is seen up to 2,000 K. Also, the exchanged Cl and O anions show no tendency to return to their original positions. Considering the high temperature and melted conditions in the actual synthesis[10], extrinsic Cl-O disorder in the anti-perovskites may occur if the heat of fusion is much higher than the enthalpy cost for the Cl-O exchange. Our results show that structural disorder is an important factor in inducing superionic conductivity. In this work, we have conducted a simple case study, and there are likely other types of structural disorder with lower formation energies. Further studies are needed to better understand this issue. We also simulated the Cl-O interchanged LOCB1 composite, and the obtained results of MSD and Li sub-lattice disorder at high temperatures are similar to those of the disordered LOC.

The activation enthalpy is deduced from the Arrhenius relation $D \propto exp(-\Delta H/k_BT)$, where D and ΔH are the diffusion coefficient for Li^+ ion transport and the activation enthalpy, respectively. Fig. 9 shows the Arrhenius plot for different diffusion coefficients from 750 to 2,000 K. From these results we obtained ΔH of 0.303, 0.311, 0.288, and 0.332 eV for LOC+V_{Li}, LOB+V_{Li}, LOCB1+V_{Li}, and LOCB2+V_{Li}, respectively. The calculated ΔH of LOC+V_{Li} and LOB+V_{Li} agree with the value of 0.2-0.3 eV determined in the experiment[10]. The calculated results for LOCB1 and LCBO2 are much

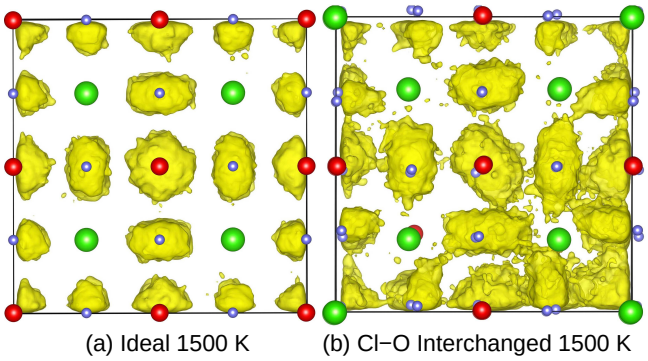

FIG. 8: (Color online) XY projection of Li trajectories (yellow) in the fixed-volume supercell at 1,500 K for the ideal and disordered LOC. The blue, red, and green spheres represent the initial positions of Li, O, and Cl, respectively.

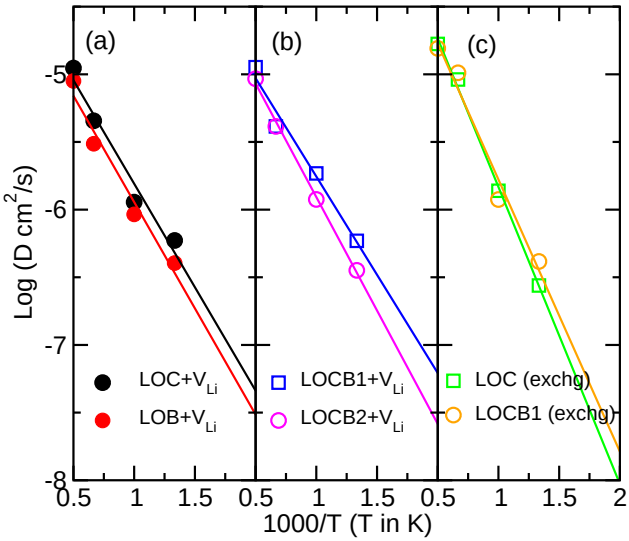

FIG. 9: (Color online) Arrhenius diffusion coefficient plot of (a) LOC+V_{Li} and LOB+V_{Li}, (b) LOCB1+V_{Li} and LOCB2+V_{Li}, and (c) disordered LOC and LOCB1 with one pair of Cl-O interchanged in the 40-atom supercell.

higher than the measured 0.18 eV for $Li_3OCl_{0.5}Br_{0.5}$[10]. A likely source for this difference is the extra disorder and vacancies introduced in the mixing process, which is not considered in our calculations. The high concentrations of disorder and vacancy and their cooperative interaction may be responsible for the reduced activation barrier. We further calculated the activation enthalpy of disordered LOC and LOCB1 with one pair of Cl-O anion interchanged. The obtained results of 0.435 and 0.399 eV are ∼0.1 eV higher than those presented above; but they are still low enough to induce fast Li^+ ion transport. Using the Nernst-Einstein equation[36], we extrapolated Li^+ ion conductivity at 300 K for LOC+V_{Li} and LOCB1+V_{Li} and obtained $0.12\times10^{-3}S/cm$ and $0.21\times10^{-3}S/cm$, respectively. These results are significantly smaller than the experimental values[10] of $0.85\times10^{-3}S/cm$ and $1.94\times10^{-3}S/cm$; however, they correctly reproduce the order (i.e., LOCB exhibits higher Li^+ ion conductivity than LOC) and the relative ratio (about 2:1). It indicates that the present theoretical modeling and calculations have captured essential physics of the observed phenomena, although more work is needed to account for the complex structural and dynamic effects beyond the current treatment for a better quantitative description.

C. Crystal and Sublattice Melting

In recently reported experiment, superionic conductivity was observed in Li_3OCl and $Li_3OCl_{0.5}Br_{0.5}$ at temperatures about 30 K below the crystal melting temperature (T_m) of 550-600 K[10]. To simulate the crystal and Li-sublattice melting, we have run more elaborate AIMD simulations that allow volume change with temperature. Fig. 10 shows the calculated MSD and volume change with temperature for LOC+V_{Li} and LOB+V_{Li}. The estimated melting temperature for LOC+V_{Li} and LOB+V_{Li} is around 500 K at which all the ions start to diffuse [See Fig. 10(a) and (b)]. The crystal melting is also supported by the drastic volume expansion at 500 K shown in Fig. 10(g). Below 500 K, we obtain a linear volume dependence on temperature, and the calculated linear thermal expansion coefficients are 2.11×10^{-5}/K and 1.82×10^{-5}/K, respectively. The volume expansion provides more space for interstitial Li^+ ions, which facilitates Li^+ ion transport. We were unable to determine the activation enthalpy here since the AIMD simulations required to extract such information would take exceedingly long time as the temperature ($<T_m$) is too low to induce measurable MSD within computationally affordable time frame. Nevertheless, we expect that the additional space produce by the thermal expansion of volume would lead to reduced activation enthalpy. From Fig. 10(c) and (d), it is seen that both LOC and LOB experience a Li sub-lattice melting stage prior to the melting of the whole crystal. Different from the crystal melting, the sub-lattice melting does not result in large volume expansions. It indicates that the anion lattice framework will remain stable when the Li sub-lattice melts. The simulated melting temperatures for Li sublattice in LOC+V_{Li} and LOB+V_{Li} are 480 and 450 K, respectively, which are 20 and 50 K below the crystal melting temperature in good agreement with the experimental observation[10]. The Li^+ ion transport in melted sub-lattice is much faster than that in the unmelted one. The corresponding Li^+ conductivities for LOC and LOB are $4.58\times10^{-2}S/cm$ and $5.36\times10^{-2}S/cm$, respectively. These results are in good agreement with the experimental data of $\sigma > 10^{-2}S/cm$ at T>523 K where the lithium sub-lattice melting occurs[10]. Below 400 K, the Li sublattice becomes stable (non-melting) and the Li^+ migration is governed by the mechanism discussed in the previous sections, and the calculated MSD_{Li} of LOC and LOB within the simulation time are too small to be

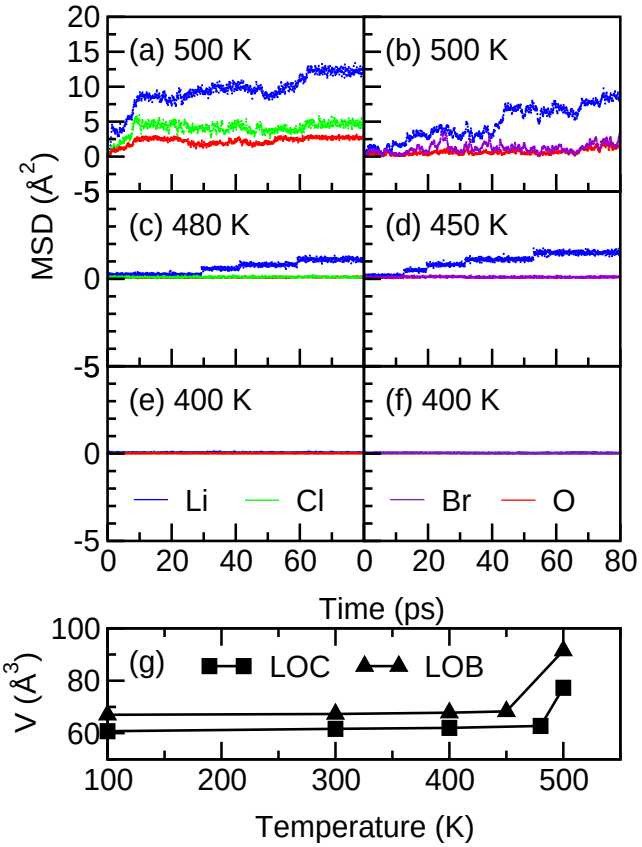

FIG. 10: (Color online) Calculated MSDs of all ion species for LOC and LOB at different stages: (a, b) melting, (c, d) sub-lattice melting, and (e, f) non-melting. (g) The volume changes of LOC and LOB as functions of temperature from the variable volume AIMD simulations.

distinguished from zero as shown in Fig.10(e) and (f). When accelerated by the elevated temperature scheme, we obtained AIMD results that are essentially the same as those shown in Fig. 5.

We have run variable volume AIMD simulations for LOCB1+V_{Li} and obtained similar results. The calculated linear thermal expansion coefficient is 4.97×10^{-5}/K, which is much larger than that of LOC and LOB. The Li sub-lattice in LOCB1 melts around 450 K, where we obtain a moderate MSD_{Li} increase of $\sim$ 0.8 $\mathring{A}^2$ in 80 ps, which is 45% smaller than that of LOB. This result does not explain the advanced superionic conduction of 10^0S/cm for $Li_3OCl_{0.5}Br_{0.5}$ in the partial melting region seen in the experiment[10]. For the Li_3OCl and Li_3OBr end-members, the measured conductivities are at least one order of magnitude smaller than that of $Li_3OCl_{0.5}Br_{0.5}$ at their sub-lattice melting stages. More complicated lattice disorders, local strains, and the cooperative interplays[37] between defects and Li^+ ions could be responsible for the unusual Li^+ ion conductivity of $Li_3OCl_{0.5}Br_{0.5}$. Further work is needed to better understand these more complicated factors.

IV. CONCLUSION

We have performed first-principles density functional theory and molecular dynamics calculations to study the stability of Li-rich anti-perovskites and the mechanisms of fast Li^+ ion transport in these materials. The phase diagram and electronic structure calculations suggest that the anti-perovskites Li_3OCl, Li_3OBr, and their mixed composite $Li_3OCl_{0.5}Br_{0.5}$ are metastable and they may exhibit excellent electrochemical stability. AIMD calculations show that the anti-perovskites with perfect crystal structures are not good Li^+ ion conductors. Li vacancies and structural disorders promote Li^+ ion migration by reducing the enthalpy barriers along the preferred pathways, resulting in the high ionic conductivities of Li_3OCl and Li_3OBr. This suggests that Li^+ ion conductivity of anti-perovskites can be effectively tuned by Li vacancy concentration and structural disorder. We performed AIMD simulations of Li^+ ion transport at the stages of non-melting, sub-lattice melting, and crystal melting, and the calculated activation enthalpies and ionic conductivities for the Li_3OCl and Li_3OBr end-members are in good agreement with experiment. However, the significantly enhanced Li^+ ion conductivity observed in the mixed $Li_3OCl_{0.5}Br_{0.5}$ composite remains unexplained. This unusual enhancement may be attributed to more complicated disorders and cooperative interplays between various defects and Li^+ ions that are not considered in the current investigation. Further studies are needed to resolve and better understand these issues. The present work provides a theoretical understanding of the fundamental physics concerning the thermodynamic and electrochemical stability and the essential mechanisms for ionic transport in the anti-perovskites, which is expected to stimulate further studies of this class of anti-perovskites and other charge-inverted materials.

V. ACKNOWLEDGMENTS

The UNLV High Pressure Science and Engineering Center (HiPSEC) is a DOE NNSA Center of Excellence supported by Cooperative Agreement DE-FC52-06NA27684. Yi Zhang would like to thank Jihui Yang and Jian-Tao Wang for helpful discussion and continuous encouragement.

[1] V. Thangadurai and W Weppner, Ionics **12**, 81 (2006).
[2] Y. Inaguma, L. Chen, M. Itoh, T. Nakamura, T. Uchida, H. Ikuta, and M. Wakihara, Solid State Commun. **86**, 689 (1993).
[3] R. Kanno and M. Murayama, J. Electrochem. Soc. **148**, A742 (2001).
[4] F. Mizuno, A. Hayashi, K. Tadanaga, and M. Tatsumisago, Adv. Mater. **17**, 918 (2005).
[5] S. Kondo, K. Takada, and Y. Yamamura, Solid State Ion. **53**, 1183 (1992).
[6] U. V. Alpen, A. Rabenau, and G. H. Talat, Appl. Phys. Lett. **30**, 621 (1977).
[7] M. O'keeffe and J. -O. Bovi, Science, **206**, 599 (1979).
[8] V. M. Bouznik, Y. N. Moskvich, and V. N. Voronov, Chem. Phys. Lett. **37**, 464 (1976).
[9] A. V. Chadwick, J. H. Strange, G. A. Ranieri, and M. Terenzi, Solid State Ion. **9-10**, 555 (1983).
[10] Y. Zhao and L. L. Daemen, J. Am. Chem. Soc. **134**, 15042 (2012).
[11] Y. Zhao, D. J. Weidner, J. C. Parise, D. Cox, Phys. Earth Planet. Inter. **76**, 17 (1993).
[12] T. J. Pennycook, M. J. Beck, K. Varga, M. Varela, S. J. Pennycook, S. T. Pantelides, Phys. Rev. Lett. **104**, 115901 (2010).
[13] A. Feinberg and C. H. Perry, J. Phys. Chem. Solids **42**, 513 (1981).
[14] J. P. Perdew, K. Burke, and M. Ernzerhof, Phys. Rev. Lett. **77**, 3865 (1996).
[15] G. Kresse and J. Furthmüller, Phys. Rev. B **54**, 11169 (1996).
[16] G. Kresse and D. Joubert, Phys. Rev. B **59**, 1758 (1999).
[17] H. J. Monkhorst and J. D. Pack, Phys. Rev. B **13**, 5188 (1976).
[18] http://theory.cm.utexas.edu/vtsttools/neb
[19] J. T. Wang, C. F. Chen, and Y. Kawazoe, Phys. Rev. Lett. **106**, 075501 (2011).
[20] J. T. Wang, C. F. Chen, and Y. Kawazoe, Phys. Rev. B **84**, 012102 (2011).
[21] G. Shen, D. Ikuta, S. Sinogeikin, Q. Li, Y. Zhang, and C. F. Chen, Phys. Rev. Lett. **109**, 205503 (2012).
[22] J. Yang and J. S. Tse, J. Phys. Chem. A **115**, 13045 (2011).
[23] Y. F. Mo, S. P. Ong, and G. Ceder, Chem. Mater. **24**, 15 (2012).
[24] A. R. Chakhmouradian, K. Ross, R. H. Mitchell, and I. Swainson, Phys. Chem. Minerals **28**, 277 (2001).
[25] http://lb.chemie.uni-hamburg.de
[26] J. Zhang, J. Han, Z. Lin, M. H. Braga, L. L. Daemen, L. Wang, and Y. Zhao, (to be published).
[27] S. P. Ong, L. Wang, B. Kang, and G. Ceder, Chem. Mater. **20**, 1798 (2008).
[28] T. W. D. Farley, W. Hayes, S. Hull, M. T. Hutchings, and M. Vrtis, J. Phys.: Condens. Matter **3**, 4761 (1991).
[29] S. P. Ong, O. Andreussi, Y. Wu, N. Mazari, and G. Ceder, Chem. Mater. **23**, 2979 (2011).
[30] J. Hedy, G. E. Scuseria, and M. Ernzerhof, J. Chem. Phys. **118**, 8207 (2003).
[31] A. Rabenau, Solid State Ion. **6**, 277 (1982).
[32] S. Wu, Z. Dong, P. Wu, and F. Boey, J. Mater. Chem. **21**, 165 (2011).
[33] S. Hull, Rep. Prog. Phys. **67**, 1233 (2004).
[34] P. A. Cheeseman and C. A. Angell, Solid State Ion. **5**, 597 (1981).
[35] N. Kamaya, K. Homma, Y. Yamakawa, M. Hirayama, R. Kanno, M. Yonemura, T. Kamiyama, Y. Kato, S. Hama, K. Kawamoto, and A. Mitsui, Nature Mater. **10**, 682 (2011).
[36] J. O′M. Bockris and A. K. N. Reddy, *Modern Electrochemistry* (Vol. 1), Plenum Press (1970).
[37] E. Kendrick, J. Kendrick, K. S. Knight, M. S. Islam, and P. R. Slater. Nature Mater. **6**, 871 (2007).